High-precision methods and devices for *in situ* measurements of thermally induced aberrations in optical elements

Victor V. Zelenogorsky, Alexander A. Solovyov, Ilya E. Kozhevatov,
Eugene E. Kamenetsky, Eugene A. Rudenchik, Oleg V. Palashov,
Dmitry E. Silin, and Efim A. Khazanov

An optical system that comprises two devices for remote measurements, a broadband optical interferometer and a scanning Hartmann sensor, is described. The results of simultaneous measurements with both devices and the results of numerical modeling of sample surface heating are presented.

OCIS codes: 120.5050, 120.3180, 120.6810.

1. Introduction

The creation of optical elements and systems with low levels of aberrations has always been a challenge that has stimulated progress in control technologies. There is, however, also an old tendency to increase average powers of lasers for basic research,[1–3] production, and military applications.[4] As a result, the need has recently arisen to use laser fields with high-quality wavefronts and high power. These requirements have drawn special attention to thermal effects that occur in optical elements. There are a number of basic problems (e.g., the design of laser interferometers for gravitational wave detection[1,2] and laser drivers for controlled nuclear fusion[3]) that cannot be solved unless these effects are considered and suppressed.

It is known that an ideal optical medium and pure dielectric coatings do not absorb radiation. Real absorption coefficients are small, and typically only their approximate values are known. Small as they are, the absorption coefficients, however, lead to quite significant effects at high powers of laser radiation. Even less is known about the character of nonuniformities, i.e., the absorption coefficients in optical materials. Nonuniform heat distribution together with low heat conductivity can cause unacceptable aberrations in optical elements.

The character of heating is also quite diverse: continuous and pulsed, surface (through heat release in coatings of optical elements) and bulk (inside the optical element). Each factor may assume different significance depending on the arrangement and purpose of the optical design. (For example, properties of reflective mirrors depend mainly on the form and properties of the surface, whereas in lenses the refractive index makes a difference as well.) Therefore it is important to have a wide arsenal of methods and means of control to be able to measure simultaneously and, when possible, in real time, all significant parameters. The methods of diagnostics should not only be remote but also not hinder operation of any elements of the system.

In this paper we report an optical system that incorporates two remote control devices: a broadband optical interferometer and a scanning Hartmann sensor. Results of numerical modeling are presented. They are in good agreement with experimental results that we obtained in our investigation of surface heating of a fused-silica sample by both devices.

2. Interferometric Techniques for *In Situ* Diagnostics

Interferometric techniques and devices have been successfully used for many years to measure optical thicknesses of media and shapes of optical element surfaces. An advantage of interferometry is that it provides two-dimensional data; i.e., the surface profile can be ob-

---

The authors are with the Institute of Applied Physics of the Russian Academy of Science, Uljanov Street 46, Nizhny Novgorod, 603950, Russia. V. Zelenogorsky's e-mail address is vvmailv@mail.ru.

Received 20 October 2005; accepted 17 December 2005; posted 24 January 2006 (Doc. ID 65490).
0003-6935/06/174092-10$15.00/0

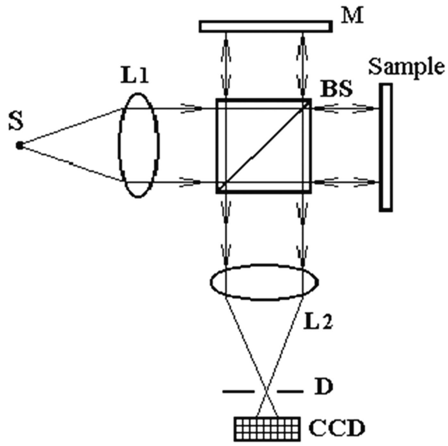

Fig. 1. Schematic of the Michelson interferometer: S, point source; L1, collimator; BS, beam splitter; M, reference mirror; D, diaphragm; L2, output objective.

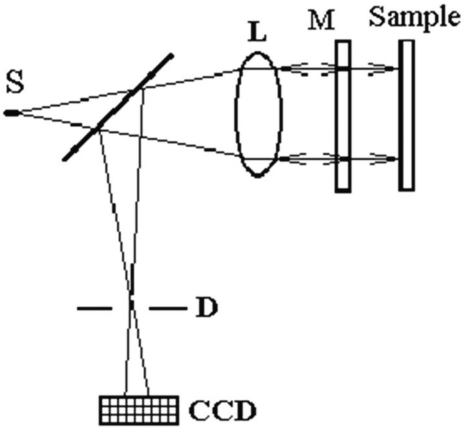

Fig. 2. Schematic of the Fizeau interferometer: L, objective.

tained simultaneously over the entire aperture of the optical element. There is an opinion that, despite all their merits, interferometers have the serious disadvantage of high sensitivity to vibrations associated with seismic and acoustic noise and to drifts caused by thermal expansion of construction elements. It might seem that this disadvantage would make the use of interferometers for remote measurements quite problematic, because elements to be measured are, as a rule, mechanically isolated from interferometer elements, and thus external seismic noise is maximally exhibited. We have developed and describe here an interferometric scheme that, to a significant degree, is free of this disadvantage because of a number of improvements that we have made.

For a better understanding of the proposed scheme, we first focus on the general principles of high-precision interferometry measurements of optical surfaces and media. An illustrative example here is that of a Michelson interferometer whose schematic is shown in Fig. 1. The interferometer includes a point source, a collimator, a beam splitter, a reference mirror, a sample, a diaphragm, an output objective, and a CCD camera.

Beams are split by the beam splitter and travel different optical paths along two spatially separated arms of the interferometer, a reference arm and a sample arm. Then the beams are reunited in the beam splitter and interfere. Objective L_2 constructs an image of the sample's surface in the interfering beams in the CCD camera. The diaphragm eliminates parasitic signals from the light flux.

If we represent the light intensity at the output of the interferometer as a product of amplitude component $A(\Delta)$ and phase component $\Psi(\Delta)$:

$$I(\Delta) = A(\Delta)\cos\Psi(\Delta), \tag{1}$$

then

$$\Psi(\Delta) = 2\pi\Delta/\lambda, \tag{2}$$

where $\Delta = \Delta(x, y)$ is the optical path difference between sample and reference arms of the interferometer and λ is the wavelength of the probing radiation. In measuring optical surface shape or optical thickness, one is typically interested only in phase component $\Psi(\Delta)$. Its value is linearly dependent on the difference between profiles of the reference and sample surfaces. A profile difference of $\lambda/2$ leads to an optical path difference of λ, owing to the double path in which the beams run. This corresponds to a 2π phase shift of the interferogram, as can be seen from Eqs. (1) and (2).

If the required measurement accuracy is $\lambda/1000$, the phase should be measured to within an accuracy of $2\pi/500$. It is hard to notice such subtle phase features merely by observing the intensity in the interference pattern because illumination nonuniformity and other factors that affect amplitude component $A(\Delta)$ are usually much stronger. Nonetheless, this problem can be successfully solved by additional modulation of the phase component by a value of $\sim\lambda/2$. Subsequent synchronous detection effectively separates contributions to the intensity [Eq. (1)] of the amplitude and phase components. This technique is called phase-shift interferometry.[5–9] It provides a measurement accuracy as high as $\lambda/1000$.[10–12] In these measurements the reference surface profile is assumed either ideal or previously known to an accuracy better than the expected measurement accuracy.

A. Specific Features of Michelson and Fizeau Interferometers

Along with the properties that the two interferometers have in common, there are also specific features that they possess because of differences in their optical design and technical solutions.

The Michelson interferometer can have a broadband light source, because one can make the optical path difference near zero by aligning the reference and sample arms. A near-zero difference can also be achieved when a sample is far away from other elements of the interferometer. However, phase noise associated with noncorrelated vibrations and fluctu-

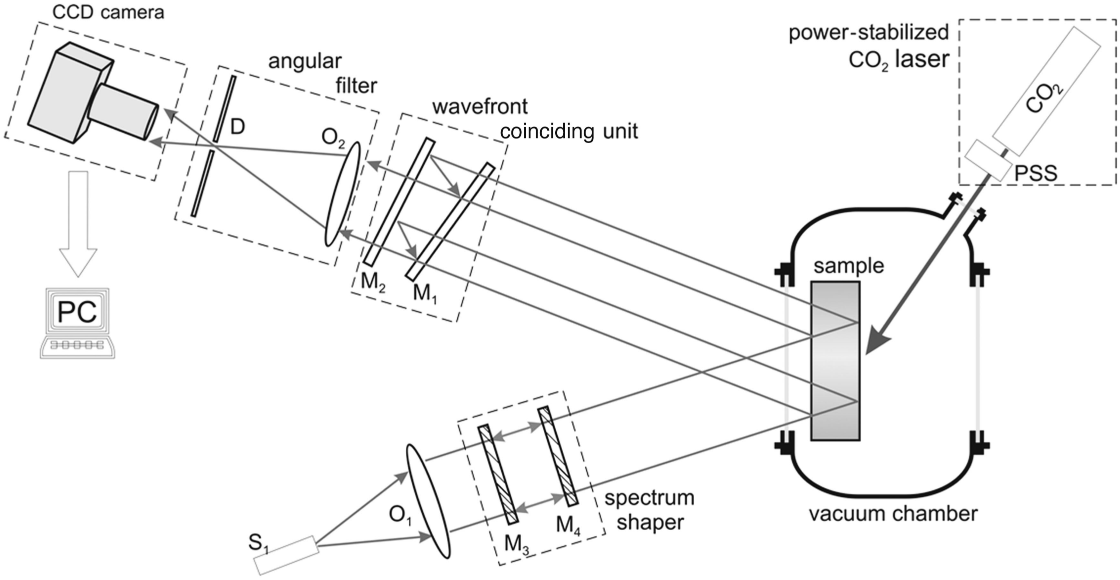

Fig. 3. Optical layout of the broadband optical interferometer: S_1, point light source, light-emitting diode; objective O_1, collimator; M_1–M_4, half-transparent flat mirrors; O_2, objective; D, diaphragm; PSS, CO_2 laser power stabilization system.

ations of the optical density of the medium in the sample and reference arms makes accurate measurements almost impossible in the Michelson interferometer. The accuracy of interferometric schemes with separated arms is typically only $\lambda/10$; see Ref. 13.

This disadvantage of the Michelson interferometer was successfully overcome in the Fizeau interferometer.[10,11,14] Its schematic is presented in Fig. 2. Here the interfering beams are separated on the working surface of a reference mirror. Despite the similarity of the Michelson and Fizeau interferometers, there is a great difference between them. In contrast to those in the Michelson interferometer, the optical paths of interfering beams in the Fizeau interferometer mainly coincide. The only region where they do not coincide is between the sample and reference surfaces. As a result, noises induced by vibrations and fluctuations of optical density of the medium become correlated in the two arms and compensate for one another to a great degree.

Unfortunately, this scheme is not free of disadvantages. If a sample is at some distance from the reference surface, the requirements for angular size of the light source and its monochromaticity become too stringent, and thus the distance between the reference surface and the sample should be kept minimal. In addition, unlike for the Michelson interferometer, which can operate with broadband sources, the high monochromaticity of radiation in the Fizeau interferometer does not permit distance selectivity of the sample's surface. A contribution to the interferogram is made by radiation reflected not only from sample surfaces but also from all other reflective surfaces along the optical axis of the interferometer. This makes application of Fizeau and Michelson interferometers for *in situ* measurements equally difficult.

B. Low-Noise Broadband Interferometer

We have proposed a number of modifications to combine the advantages of the Michelson interferometer (i.e., a broadband light source and distance selectivity along the line of sight) and of the Fizeau interferometer (high stability to noise)[10–12,15] while using the well-known phase-shift interferometry technique. We have introduced two additional devices into the interferometric scheme: a spectrum shaper and a wavefront coinciding unit.

Expression (2) shows that one can perform phase modulation of an interferogram not only by modulating the distance between the sample and reference surfaces but also by varying the wavelength.

In fact, the possibilities for manipulating the spectral content of probing radiation are much wider. To demonstrate this, we use the fact that the functions that describe the radiation spectrum and its interferogram are Fourier conjugated.[16] This results, for instance, in the well-known fact that broadband radiation corresponds to a fast-damping interferogram. In this case estimations of the interferogram's width are valid:

$$\delta = \lambda_0(\lambda_0/\Delta\lambda), \tag{3}$$

where λ_0 is the mean wavelength and $\Delta\lambda$ is the spectrum width. At $\Delta\lambda \sim \lambda$ the interferogram exists only at distances of $\sim\lambda$, i.e., near zero.

However, according to the transfer theorem, if a spectrum is multiplied by a function with period $\delta\lambda$, i.e., by $\cos(2\pi\lambda/\delta\lambda)$, the interferogram will not be equal to zero not only at zero path differences but also at optical path differences obtained from the expression

$$\Delta = \lambda_0(\lambda_0/\delta\lambda). \tag{4}$$

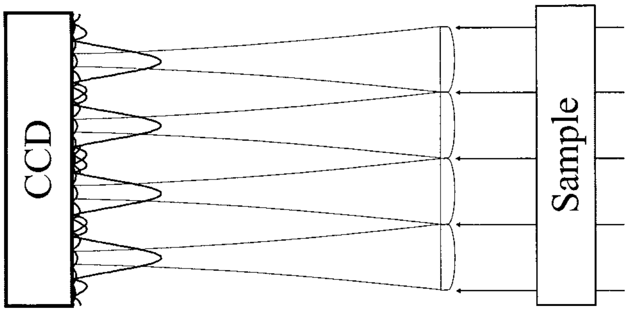

Fig. 4. Shack–Hartmann sensor.

The interval at which the interferogram contrast is nonzero is again determined by formula (3).

Thus manipulating the spectral content of the probing radiation offers three beneficial possibilities for interferometry measurements:

1. To select at one's own discretion the length of optical spacings at which interference occurs. This permits selective study of surfaces placed in an arbitrary order along the line of sight. The required length of the optical spacing is determined by period $\delta\lambda$, with which the spectrum of the probing radiation should be modulated.
2. To set the degree of selectivity of the interferogram with respect to the optical spacing being studied. The range of spacings at which the interferogram exists is determined by the spectrum width of probing radiation $\Delta\lambda$.
3. To modulate the interferogram phase without modulating distances between the sample and reference surfaces. The modulation is made as a result of time modulation of λ_0.

Let us discuss in more detail the specific features of the interferometer scheme that we propose here. Its optical layout is presented in Fig. 3. The source of the probing radiation is a light-emitting diode. The central wavelength is $\lambda_0 = 630$ nm; the spectral width is $\Delta\lambda = 20$ nm. Objective O_1 forms collimated radiation with a plane wavefront. A spectrum shaper is an air low-Q-factor Fabry–Perot etalon that has the possibility of modulating and readjusting the air space between mirrors. During the readjustment, the maximum amplitude of the signal corresponds to mutual conjugation of the period of spectrum modulation with the optical path difference of the interfering beams. When they are fully readjusted, the positions of mirrors M_3 and M_4 become fixed, and the spectrum shaper starts operating in the phase modulation mode.

A sample was an optical element 80 mm in diameter with flat faces at an $\sim 10^{-2}$ rad angle relative to each other. By virtue of specificity of the scheme, the probing radiation is incident onto the sample's surface at an angle of ~10°.

Then the radiation is reflected from both faces of the sample and comes to the wavefront coinciding unit. In this case the beams should be matched in cross section and angle because of the wedge between the sample faces. The match can be made by mirrors of the spectrum shaper. Mutual deviation of the rays over a beam's cross section are compensated for by simultaneous turning of mirrors M_1 and M_2, while angular displacements between the beams are compensated for by the angles between working surfaces of the mirrors.

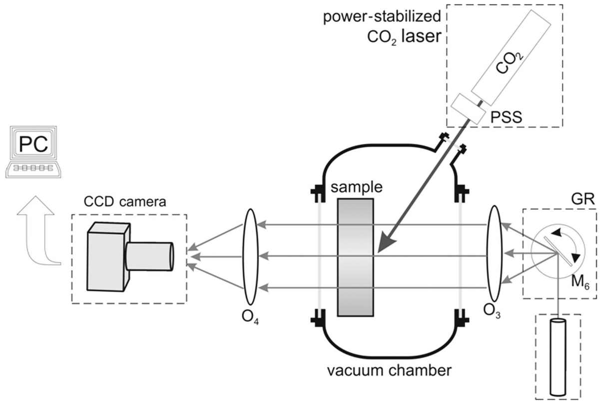

Fig. 5. Scanning Hartmann sensor: GR, galvanometer-based rotator.

The beam detector was a Mintron MS-168BP camera, a typical general-purpose 25 frame/s CCD camera. The phase-shifting algorithm for calculating the interferogram's phase required that 12 frames of the interferogram be captured at different spacings between mirrors M_1 and M_2. Thus a single measurement of phase distribution took 0.5 s.

The proposed scheme ensures a high degree of correlation of possible vibration-induced phase noises and therefore their mutual compensation. To measure thermal distortions in a sample we subtracted the phase profile of an unheated sample from the profile of a heated sample. In this case optical surface profiles do not influence measured value, and sensitivity is limited by the instability of mechanical and optical elements, electronic noises, and the turbulence of air along the optical trace. Although the distance between the sample and the interferometer elements was ~1.5 m, proposed modifications allowed us to get a measurement repeatability at a level of ~0.6 nm, i.e., $\lambda/1000$.

3. Scanning Hartmann Sensor

The Hartmann sensor was initially devised to measure concave spherical and aspherical mirrors.[17] A point light source illuminated a spherical mirror, before which a screen with multiple holes was placed. The light transmitted through the screen holes was incident onto a photosensitive paper. The positions of bright spots corresponding to the screen holes on the paper indicated the curvature of the mirror.

In 1971 Shack[18] modified this sensor by using an array of lenses instead of the screen holes (see Fig. 4). Recent Shack–Hartmann sensors incorporate a CCD matrix placed at the focus of the microlenses. The CCD matrix is meant to determine the positions of the beams focused by a set of identical microlenses. In modern commercial sensors, the wavefront measurement accuracy reaches λ/100.[19] The boundaries between lenses cause beam broadening owing to the presence of diffraction rings (Fig. 4), hence reducing the dynamic range of the sensor. The scanning Hartmann sensor is free of this disadvantage.

To study thermal effects we used the modification of the Hartmann sensor shown in Fig. 5.[20–22] In contrast to the traditional sensor, we employ a thin laser beam successively moving over a sample's surface (this explains the word scanning in the term scanning Hartmann sensor).

To move a probing beam over a sample's surface we use a high-precision galvanometer-based optical scanner (Cambridge Technology, Inc., Model 6450) that rotates mirror M_6. The mirror rotation axis passes through the focus of lens O_3. The mirror's rotation causes a parallel shift of the probing beam in the region between lenses O_3 and O_4. A CCD camera captures a two-dimensional intensity distribution of probing light in the focal plane of lens O_4. An image from the CCD camera comes to a video capture card in a computer. By shifts of this distribution an angular deviation of the scanning beam transmitted through the sample is determined. From the variety of shift-determination approaches (shifting of bisector points,[23] shift of the maximum, etc.) we have chosen one in which the shift is determined by changes in the coordinate of the center of mass of the intensity distribution. Note that, before calculations, we null out values in the regions where brightness is less than some threshold value exceeding the level of eigennoise of the CCD camera. This cutting makes the algorithm more noise immune, because the coordinates of the center of mass are strongly dependent on measurement errors at the periphery of the distribution. To increase measurement accuracy, we performed averaging over 15–20 frames (0.6, . . . , 0.8 s). As a result, the noise level was significantly reduced. Averaging over a larger number of frames did not result in noise reduction because of low-frequency divergence of noise spectra caused by air turbulence. To have an acceptable ratio between measurement time and spatial resolution, we took data from 40–50 points in the scanning interval (≈30 mm). At the recording rate of 25 frames/s that the CCD camera and video-capturing card could provide, the total time for a single scan was 25–30 s.

To prevent many systematic errors we used a differential measurement method. In this case every measurement consists of two steps. The sample is scanned first when it is cold and then during exposure to CO_2 laser radiation. Subtracting results obtained in each step, we can separate deviations of the probing beam associated with thermal effects only and calculate the respective wavefront distortions. Indeed, if $x_{1,i}$, $x_{2,i}$, $i = 1, \dots, N$ are beam coordinates on the CCD camera during the first and second measurements by the Hartmann sensor at the ith point in the scan, the angular distribution of phase-front changes is calculated from the formula

$$\alpha_i = (x_{2,i} - x_{1,i})/F_3,$$

where F_3 is the focal length of lens O_3. Integrating values of α_i over the scan length, we easily obtain the wavefront deviation:

$$w_i = 0,$$

$$w_i = \sum_{j=1}^{N} (\alpha_{j-1} + \alpha_j)\,\frac{h_x}{2}, \qquad i > 1,$$

where h_x is a scan step over the aperture.

The differential method helps to prevent many systematic errors. Specifically, we can avoid aberrations in lenses O_3 and O_4, which lead to beam's moving in the plane of the CCD camera at rotation of mirror M_6 even when there is no sample. In addition, noncoincidence of the rotation axis of this mirror with its reflective plane also does not induce any measurement errors. In some cases the systematic errors may exceed the effects being measured by several times. However, they are additively included in measurement results and depend only insignificantly on thermal changes in the sample. This permits efficient elimination of their influence on measurement. Therefore the measurement approach that we have used allows us to employ standard optics easily without jeopardizing measurement accuracy.

4. Numerical Modeling

We have developed a computer program to simulate numerically the heating, deformation, and resultant wavefront distortions of optical beams passing through a transparent sample. The temperature field of the sample is described by the thermal conductivity equation

$$C_p\rho\,\frac{\partial T(\mathbf{r})}{\partial t} = \kappa\nabla^2 T(\mathbf{r}) + q(\mathbf{r}, t), \tag{5}$$

where $T(\mathbf{r})$, C_p, ρ, and κ are the temperature, thermal capacity, density, and thermal conductivity coefficient, respectively, and $q(\mathbf{r}, t)$ is the bulk density of the heat release power. The boundary conditions are a mathematical expression of Fourier's law of heat conduction and of the heat exchange law (for vacuum it is the Stephan–Boltzmann law)[24,25]:

$$\kappa\,\frac{\partial T(\mathbf{r})}{\partial \mathbf{n}_0} = -\sigma\varepsilon[T(\mathbf{r})][T(\mathbf{r})]^4 + q_s, \qquad \mathbf{r} \in S, \qquad t > 0, \tag{6}$$

where $\mathbf{n}_0 = \mathbf{i}n_1 + \mathbf{j}n_2 + \mathbf{k}n_3$ is the unit vector in the direction of the outer surface-normal line, $\sigma = 5.67 \times 10^{-8}$ W/(m^2 K^4) is the Stephan–Boltzmann constant, $\varepsilon(T)$ is the grayness factor of the emitting sur-

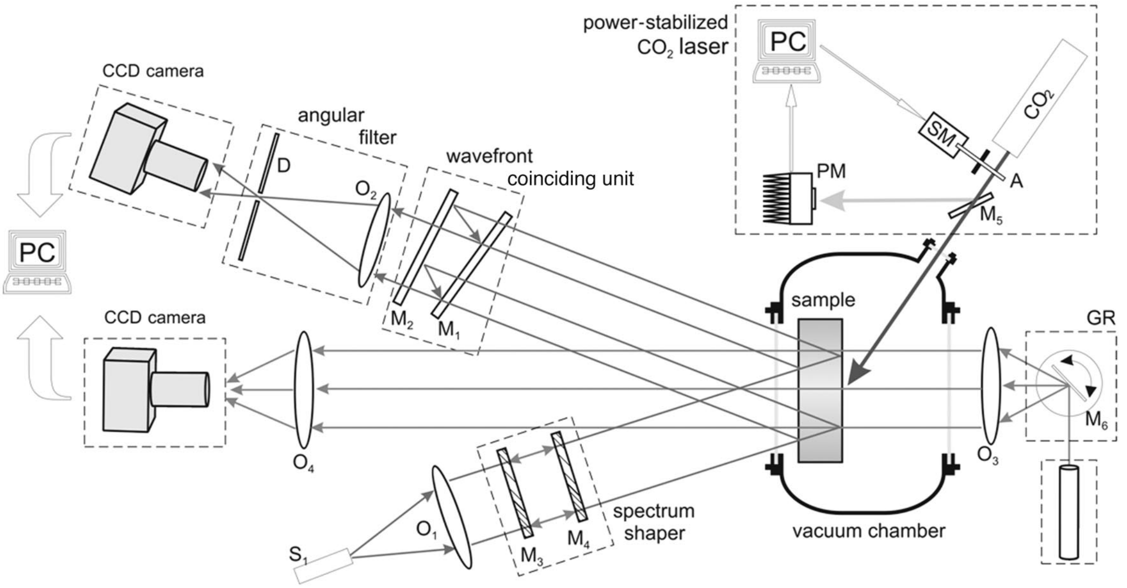

Fig. 6. Optical layout of the experimental setup: S_1, point light source; O_1, O_2, objectives; M_1–M_4, flat semitransparent mirrors; D, diaphragm; O_3, O_4, lenses; M_6, rotating mirror; M_5, salt plate; A, controllable mechanical attenuator; SM, stepper motor moving the attenuator; PM, powermeter.

face, and q_s is the surface density of the heat release power.

Equation (5) with boundary conditions (6) was approximated by the difference relations on a cylindrical grid. By considering the cylindrical symmetry we were able to reduce the relations obtained to a set of linear equations that can be solved exactly by a direct method known as the matrix backward sweep method.[26] A spatial step of the grid was determined based on the following considerations: The grid step is assumed adequate to the problem being solved if for the stationary state case the heat flow power removed from the cylinder boundaries owing to heat exchange by not more than 1% differs from a given power of heating laser radiation. A temporal step is varied, depending on the rate of temperature change (the higher the rate, the smaller the step). If the calculation error is less than 1%, the discretization is thought to be adequate.

Then we calculated sample deformations. The static of an elastic nonuniformly heated body is described by the following equation[27]:

$$\mu \Delta \mathbf{U} + (\lambda + \mu) \nabla (\nabla \mathbf{U}) = \alpha_T \left(\lambda + \frac{2}{3} \mu \right) T, \tag{7}$$

where α_T is the coefficient of linear thermal expansion, $\mathbf{U}$ is the deformation vector, and λ and μ are Lame coefficients. The vector that satisfies Eq. (7) unambiguously determines deformation tensor U^{ij} by the following relation[27]:

$$U^{ik} = \frac{1}{2} \left(\frac{\partial U_i}{\partial r_k} + \frac{\partial U_k}{\partial r_i} \right). \tag{8}$$

The boundary conditions are written for the absence of normal and shearing stress components on the sample's walls:

$$\sigma_{ik} n_k = 0 \tag{9}$$

for $i = 1, \ldots, 3$; σ_{ik} is the stress tensor. Here and further in the text a summation over a dummy index is implied. The expression that connects deformation tensor U^{ij} and stress tensor σ_{ik} is written as follows[27]:

$$\sigma_{ij} = 2\mu U^{ij} + \left[\lambda U^{kk} - \left(\lambda + \frac{2}{3} \mu \right) \alpha T \right] \delta_{ij}. \tag{10}$$

The finite-difference approximation of Eq. (7) with boundary conditions (9) led to a set of linear equations that were solved iteratively by the alternating-triangular method.[26]

The distribution of the temperature and of the deformation field of the sample allows us to calculate changes in the optical path length of the beam passing through the sample. We used the following formula[28]:

$$\Delta L_i = \int_0^l \left[-\frac{1}{2} n^3 \pi_{iikl} \sigma_{kl} - \frac{\beta T}{{n_0}^3} + (n-1) U^{zz} \right] \mathrm{d}z, \tag{11}$$

where n is the refractive index of sample points before heating, $\beta = \mathrm{d}n/\mathrm{d}T$ is the thermal coefficient, π_{iikl} is the tensor of piezo-optic coefficients, and L is the thickness of the sample. Equation (11) treats in a linear approximation both the temperature dependence of the refractive index and sample deformation including the photoelastic effect. The first term on the

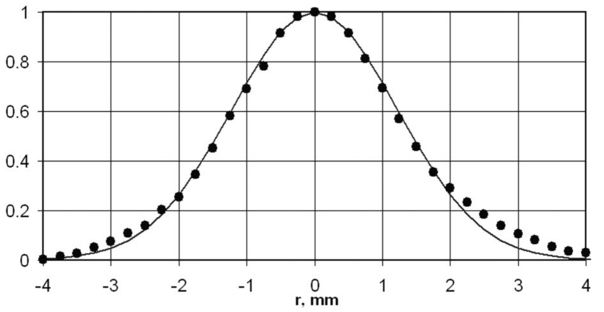

Fig. 7. Transverse intensity distribution of CO_2 laser beams (points) and Gaussian function (solid curve).

right-hand side of Eq. (11) is responsible for the photoelastic effect (note that in contrast to other components it considers induced birefringence); the second term, for the temperature dependence of the refractive index of the medium; the third term, for the change of geometrical sizes of the sample that occur with temperature changes.

Using the developed program, we numerically modeled heating of a cylindrical sample placed in vacuum, i.e., under conditions of radiant heat exchange. Surface heating from a heat source with a Gaussian intensity distribution located at the surface of one of the faces of the sample was modeled.

Comparison of calculated curves for axially symmetric wavefront distortions with experimental results (see Section 5 below for details) shows that this mathematical model describes well thermal distortions in cylindrical optical elements.

5. Experimental Results

A schematic of the experimental setup is shown in Fig. 6. It consists of the following main units: a vacuum chamber with a sample inside; a CO_2 laser, the source of surface heating; measurement devices, i.e., the broadband optical interferometer (Subsection 2.B) and the scanning Hartmann sensor (Section 3); and a computer with appropriate software.

Samples were placed in a vacuum chamber with transparent windows (Fig. 6). The chamber dimensions as well as sizes and quality of the windows were such that we could study samples with diameters of as much as 120 mm. A pump and pressure control devices provide and maintain vacuum in a pressure that ranges as much as 10^{-3} Torr. This pressure range is sufficient to provide conditions only for radiant thermal release of the sample.

Experimental modeling of thermal regimes at which heat is released on a sample's surface is of interest because it reconstructs conditions of the heating of mirrors by high-power laser radiation. These conditions can easily be achieved by use of CO_2 laser radiation (Fig. 6) at 10.6 μm, which is absorbed in a superficial (several micrometers) surface layer of many optical materials, such as glass and fused silica.

The CO_2 laser employed in our experiment was equipped with a power stabilization system that we have developed by using a controllable mechanical attenuator. The attenuator consists of a disk shutter with a slot width that depends on the distance to the center of rotation. By moving the rotating shutter disk with respect to the beam, we can control the average power of passing radiation. The movement was made by a computer-controlled stepper motor. Part of the laser radiation passing through the attenuator was directed with a salt plate to a Gentec UP19K IR-light powermeter. A signal from the powermeter went to an analog-to-digital converter at the computer. The computer processed this signal and controlled the attenuator, thus completing the feedback.

To perform numerical modeling, one needs to know the transverse distribution of the heat source. It was measured in the following way: A CO_2 laser beam was scanned by a vertical slot diaphragm. A powermeter placed behind the diaphragm measured the power of laser radiation passing through the diaphragm. The width of the diaphragm is much less than the beam width, so, when a Gaussian beam is scanned, the curve will be of the same width. The results of scanning CO_2 laser radiation and the respective Gaussian function are illustrated in Fig. 7. The figure shows that the beam's intensity distribution is nearly Gaussian.

The samples were fused-silica cylinders with a diameter of 100 mm and a thickness of 25 mm. We performed a series of repeated measurements of the sample in the stationary state at room temperature, using the scanning Hartmann sensor and the optical interferometer. Our aim was to determine the noise of our devices. At the same time, we checked that the sample was in the stationary state. An interferogram of the sample in the stationary state is presented in Fig. 8(a).

Before heating the sample, we interferometrically measured the distribution of optical thickness for a few minutes. In addition, a first series of measurements with the scanning Hartmann sensor was performed. Then we used the CO_2 laser to heat the sample, not terminating the interferometric measurements so that we could observe how the thermal lens occurs and develops. Once the stationary state was set up [Fig. 8(b)], a second series of measurements with the scanning Hartmann sensor was performed. Then we blocked the CO_2 laser radiation and observed the process of sample cooling and relaxation of the profile of the optical thickness to its initial state.

In interferometric measurements, we obtained information on phase distribution by processing 12 frames at a capture rate of 25 Hz. The characteristic time of a single measurement was ~0.5 s. Because this time was so short compared with the time of thermal lens development and setup (a few minutes), we could continuously observe the process of distortion formation in the sample. Measurements with the scanning Hartmann sensor were made only when the sample was in the stationary state.

The acquisition of the temporal sequence of two-dimensional distribution of the sample's optical

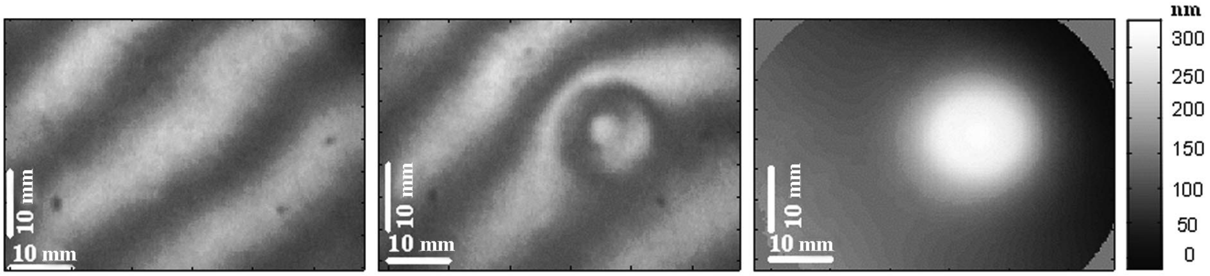

(a) (b) (c)

Fig. 8. Interferograms of stationary states of the sample (a) not heated and (b) heated by the CO_2 laser and (c) profile of the heating-induced change in the optical thickness of the sample.

thickness with high spatial and time resolution clearly demonstrated the spatiotemporal characteristics of noises of our interferometric measurement and permitted us to measure the dynamics of optical distortions caused by the thermal effects. Experiments showed that the temporal noise of the interferometer did not exceed 0.6 nm, as evaluated by root-mean-square deviations.

As every series of scanning Hartmann sensor measurements of the sample in each stationary state consisted of several measurements, we could evaluate the accuracy of the sensor. Experiments showed that it is 5–10 nm.

Further analysis demonstrated that an essential factor in determining the noise of our measurement devices was fluctuations of the refractive index of the medium along the path from the sample to the devices. In our experiments this distance was 1.5 m. Better sensitivity of the optical interferometer can be accounted for by good coincidence of the optical paths of interfering beams from the sample to the CCD camera. In the scanning Hartmann sensor measurements, the effect of fluctuations of the refractive index of air was more dramatic.

Note that in our experiments the probe radiation of the scanning Hartmann sensor passes through the sample, whereas in the interferometric measurements the trial radiation is reflected from the sample. As a result, physical quantities measured by these devices are different. The scanning Hartmann sensor measures wavefront phase distributions of the radiation passing through the sample (ϕ), whereas the optical interferometer measures the distribution of the optical thickness of the sample (h). In the simplest case, these values can be calculated as

$$\phi = (n - 1)L, \qquad h = nl,$$

where L is the thickness of the sample. Changes of these values that occur because of irradiation of a sample in the approximation of uniform temperature distribution over the sample's thickness can be written in the form

$$\Delta\phi = [P + (n_0 - 1)\alpha_T]L\Delta T, \qquad \Delta h = (P + n_0\alpha_T)L\Delta T, \tag{12}$$

where[21]

$$P = \beta - \alpha_T \frac{n_0^{\,3}}{4} \frac{1 + \nu}{1 - \nu} (p_{11} + p_{12})$$

and n_0 is the refractive index for $T = T_0$.

Expression (12) shows that, if α_T is much less than P, the values measured by both devices are similar. It can easily be shown that this conclusion is valid for nonuniform temperature distribution as well. For fused silica, P is 20 times higher than α_T ($\beta = 100 \times 10^{-7}\,\mathrm{K}^{-1}$, $P = 98 \times 10^{-7}\,\mathrm{K}^{-1}$, and $\alpha_T = 5 \times 10^{-7}\,\mathrm{K}^{-1}$).

Figure 9 presents the results of an experiment in which a fused-silica sample surface was heated by CO_2 laser radiation with powers of 30 and 85 mW. The sample had no optical coating. The results obtained with the scanning Hartmann sensor (thick dashed curves in Fig. 9) and optical interferometer (thick solid curves) coincide fairly well. This figure also shows the calculated curves (thin dashed and thin solid curves) for the quantities measured by both

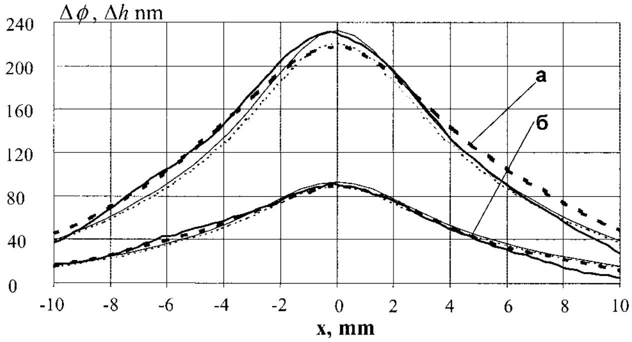

Fig. 9. Experimental results (thicker curves) and numerical modeling (thinner curves) of changes of optical thickness measured by the optical interferometer (solid curves) and changes of phase front measured by the scanning Hartmann sensor (dashed curves) at surface heating of a fused-silica sample by CO_2 laser radiation with powers (a) 85 and (b) 30 mW along horizontal axis x.

devices. In our calculations we assumed a Gaussian distribution of heat sources.

The coincidence of experimental results obtained by the two different methods with the results of numerical modeling confirms the validity of the results. The noncoincidence of data obtained with the scanning Hartmann sensor and those with the optical interferometer is explained by the fact that, though the relation $P/\alpha_T \cong 0.05$ is small, it is still not zero. A small noncoincidence between calculated and experimental results is due to a nonideal (non-Gaussian) intensity profile of the CO_2 laser beam.

6. Conclusions

In this paper we have discussed two high-precision devices for measurement of thermally induced wavefront distortions. We also gave a retrospective look at their analogs and described in detail their improvements, which may in our opinion break stereotypes regarding the accuracy and applicability of various wavefront distortion measurement techniques. For instance, there is a strong belief that, from the standpoint of measurement accuracy, the device of choice for remote control of subtle aberration effects is a Hartmann sensor rather than an optical interferometer. We have demonstrated that our modified interferometric technique provides a comparable or even higher measurement accuracy.

An advantage of the scanning Hartmann sensor is that it does not require a reference surface. In addition, the dynamic range of the scanning Hartmann sensor is much wider than in optical interferometers because it can easily be adjusted by the focal length of the objective.

Because of the improvements that we have made, the measurement accuracy of both devices has been considerably increased. The experimental accuracy was within 0.6 nm for the optical interferometer and within 5–10 nm for the scanning Hartmann sensor. Comparison of the experimental data with numerical modeling showed good coincidence.

Simultaneous measurements of phase-front deformations of radiation transmitted through a sample (scanning Hartmann sensor measurements) and reflected from sample surfaces (optical interferometer measurements) provide additional information that allows us to differentiate between the effects of mechanical deformation of optical elements and the effects of changes of the refractive index of a medium. This ability can be helpful because in lenses and mirrors the influence of these effects on the characteristics of the optical scheme can be different. Therefore it is reasonable to use both devices when one is studying the optical properties of samples, with one device utilizing transmitting radiation and the other, reflected radiation.

The study was supported by Russian Foundation for Basic Research (grant 04-02-08086) and the U.S. National Scientific Foundation (grant PHY-0244902).

References

1. J. Degallaix, C. Zhao, J. Li, and D. Blair, "Thermal lensing compensation for AIGO high optical power test facilities," Class. Quantum Grav. **21,** 903–908 (2004).
2. A. Abramovici, W. E. Althouse, R. W. P. Drever, Y. Gursel, S. Kawamura, F. J. Raab, D. Shoemaker, L. Sievers, R. E. Spero, K. S. Thorne, R. E. Vogt, R. Weiss, S. E. Whitcomb, and M. E. Zucker, "LIGO—the Laser-Interferometer-Gravitational-Wave Observatory," Science **256,** 325–333 (1992).
3. M. Yamanaka, H. Matsui, Y. Kawada, R. Kandasamy, T. Eguchi, T. Kanabe, M. Nakatsuka, Y. Izawa, S. Nakai, T. Kawashima, Y. Okada, T. Kanzaki, H. Miyajima, M. Miyamoto, and H. Kan, "Laser-diode pumped 10J × 10Hz Nd: glass slab laser for inertial fusion energy," paper TuO2cl 199 presented at the First International Conference on Inertial Fusion Sciences and Applications, Bordeaux, France, 12–17 September 1999.
4. J. Hecht, "Laser weapons go solid-state," Laser Focus World **40,** 61 (2004).
5. G. S. Gorelik, "On application of the modulation method to optical interferometry," Dokl. Akad. Nauk USSR **83,** 549–552 (1952).
6. O. Sasaki and H. Okazaki, "Sinusoidal phase modulating interferometry for surface profile measurements," Appl. Opt. **25,** 3137–3140 (1986).
7. M. Adachi, H. Miki, Y. Nakai, and I. Kawaguchi, "Optical precision using the differential method," Opt. Lett. **12,** 792–796 (1987).
8. Y. Y. Cheng and J. C. Wyant, "Phase shifter callibration in phase-shifting interferometry," Appl. Opt. **24,** 3049–3052 (1985).
9. S. W. Kim, M. G. Kang, and G. S. Han, "Accelerated phase-measuring algorithm of least squares for phase-shifting interferometry," Opt. Eng. **36,** 3101–3106 (1997).
10. A. G. Olszak, E. Novak, K. Stumpe, and J. Semrad, "High-performance interferometer for site flatness inspection," in *Interferometry '99: Applications,* P. Krzysztof and P. J. Werner, eds., Proc. SPIE **3745,** 408–415 (1999).
11. E. Novak, A. G. Olszak, K. Stumpe, R. E. Knowlden, L. Malevanchik, and G. Z. Angeli, "Laser Fizeau interferometer for silicon wafer site flatness testing," in *Surface Characterization for Computer Disks, Wafers, and Flat Panel Displays,* J. C. Stover, ed., Proc. SPIE **3619,** 101–109 (1999).
12. I. E. Kozhevatov, E. A. Rudenchik, N. P. Cheragin, and E. H. Kulikova, "Absolute testing of the profiles of large-size flat optical surfaces," Radiophys. Quantum Electron. **44,** 575–581 (2001).
13. G. E. Sommarggren, "Diffraction methods raise interferometer accuracy," Laser Focus World **32,** 61 (1996).
14. I. E. Kozhevatov, E. A. Rudenchik, N. P. Cheragin, and E. H. Kulikova, "A new remote method for estimating the parameters of optical elements," in *International Quantum Electronics Conference* (*IQEC*) (2002), p. 147.
15. I. E. Kozhevatov and E. H. Kulikova, "High-order broadband optical interferometry," Radiophys. Quantum Electron. **46,** 65–72 (2003).
16. R. J. Bell, *Introduction to Fourier Spectroscopy* (Mir, 1975).
17. J. Hartman, "Bemerkungen uber den Bau und die Justirung von Spektrographen," Z. Instrumentenkd. **20,** 47 (1900).
18. R. Tyson, *Principles of Adaptive Optics,* 2nd ed. (Academic, 1998).
19. WaveFrontSciences, "CLAS-2D data sheet" (WaveFront Sciences, Albuquerque, N.M., 2002).
20. A. K. Potemkin, A. I. Makarov, and A. N. Mal'shakov, "Measurement of small wavefront distortions of laser radiation," Opt. Spectrosc. **86,** 148–152 (1999).
21. E. A. Khazanov, N. F. Andreev, A. N. Mal'shakov, O. V.

Palashov, A. K. Poteomkin, A. M. Sergeev, A. A. Shaykin, V. V. Zelenogorsky, I. Ivanov, R. S. Amin, G. Mueller, D. B. Tanner, and D. H. Reitze, "Compensation of thermally induced modal distortions in Faraday isolators," IEEE J. Quantum Electron. **40,** 1500–1510 (2004).

22. A. K. Potemkin, A. N. Mal'shakov, N. F. Andreev, and D. H. Reitze, "Use of self-focusing for measurements of ultrasmall (less than $\lambda/3000$) wave-front distortions," J. Opt. Soc. Am. B **19,** 650–655 (2002).
23. C. Magnan and J. C. Pecker, "Asymmetry in solar spectral lines," Highlights Astron. **3,** 171–203 (1973).
24. N. M. Belyaev and A. A. Ryadno, *Methods of Thermal Conductivity Theory, Part 2* (Higher School, Moscow, 1982).
25. L. D. Landau and E. M. Lifshitz, *Theoretical Physics. Fluid Mechanics.* (Science, Moscow, 1987).
26. A. A. Samarsky and P. N. Vabishevich, *Numerical Methods for Solving Inverse Problems of Mathematical Physics* (USSR, Moscow, 2004).
27. L. D. Landau and E. M. Lifshitz, *Theoretical Physics. Theory of Elasticity* (Science, Moscow, 1987).
28. W. Koechner, *Solid-State Laser Engineering* (Springer-Verlag, 1999).